

Supplementary information

Quick-XAFS and Raman monitoring of activation, reaction and deactivation of NiCu catalysts obtained from hydrotalcite-like Precursors

Aline Ribeiro Passos^{1,3}, Camille La Fontaine¹, Sandra Helena Pulcinelli², Celso Valentim Santilli², Valérie Briois¹

- (1) SOLEIL synchrotron, L'Orme des Merisiers, BP48, 91192 Gif sur Yvette, France
- (2) Chemistry Institute of the São Paulo State University, UNESP, 14800-060, Araraquara, SP, Brazil
- (3) Brazilian Synchrotron Light Laboratory (LNLS), Brazilian Center for Research in Energy and Materials (CNPEM), 13083-970, Campinas, SP, Brazil.

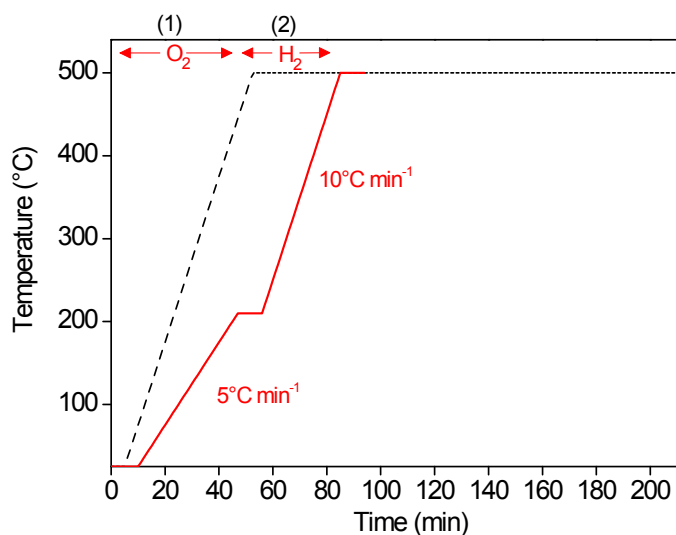


Fig. S1 Red curve indicates the temperature and the gas atmosphere protocol used for the LDH thermal decomposition (1) oxidative and (2) reductive step. The black curve represents the conventional activation process of a pre-calcined sample (at 500 °C) under H₂ for comparison purpose.¹

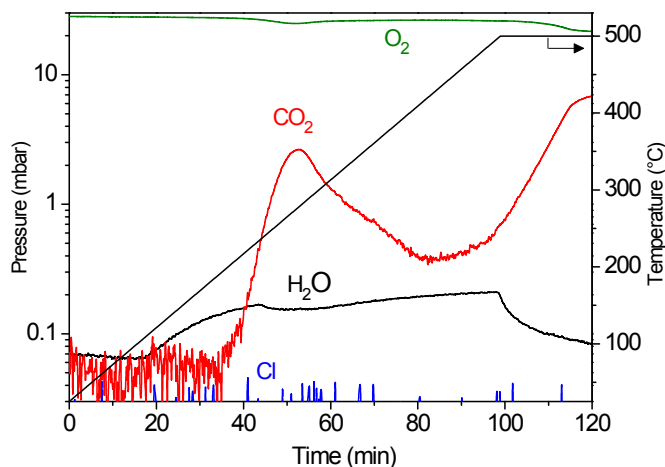


Fig. S2 Evolution of products during calcination of LDH precursor under air.

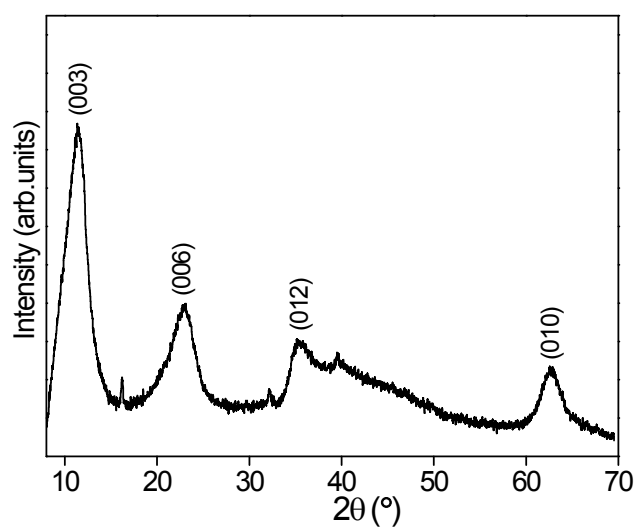


Fig. S3 XRD patterns of the as-synthesized NiCu LDH sample.

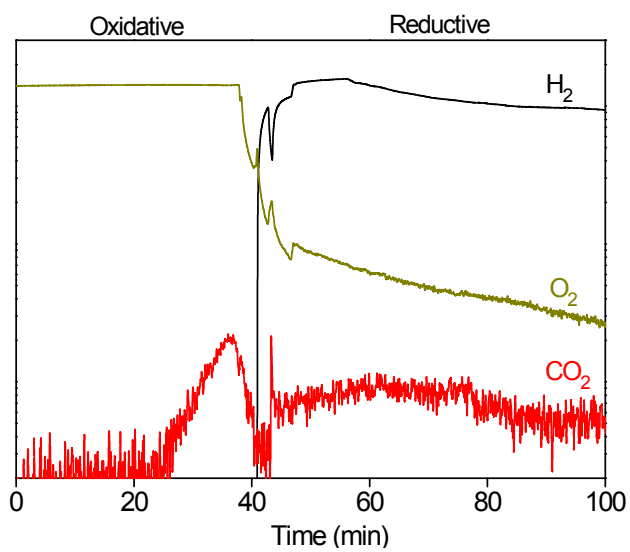


Fig. S4 Evolution of O₂, H₂ and CO₂ during the oxidative and reductive steps of thermal decomposition of the NiCu LDH precursor.

Evaluation of the number of components in the XAS data set by Principal Component Analysis and MCR-ALS analysis performed on the data set recorded during calcination and activation of the bimetallic catalyst precursor.

Methods used for estimation of the most appropriate number of components for a data set are based on Principal Component Analysis (PCA)² using the Singular Value Decomposition algorithm. The methodology is detailed in ³. Two plots are used for this purpose: the **Scree plot** which displays the eigenvalue associated to each principal component in descending order *versus* the number of components and the **Score Trajectory plot** as a function of the number of spectra contained in the data set. The number of components required to explain most of the variance of the data set is estimated with the Scree plot considering the slope break between the straight line formed by the first components and the asymptotic line passing through the other components of lower eigenvalues. The Scree plot can be used regardless the structure of the matrix D. For process-like data where data were ordered in time, temperature ..., trajectories along the reaction coordinates are expected for the scores of the components which are significant.

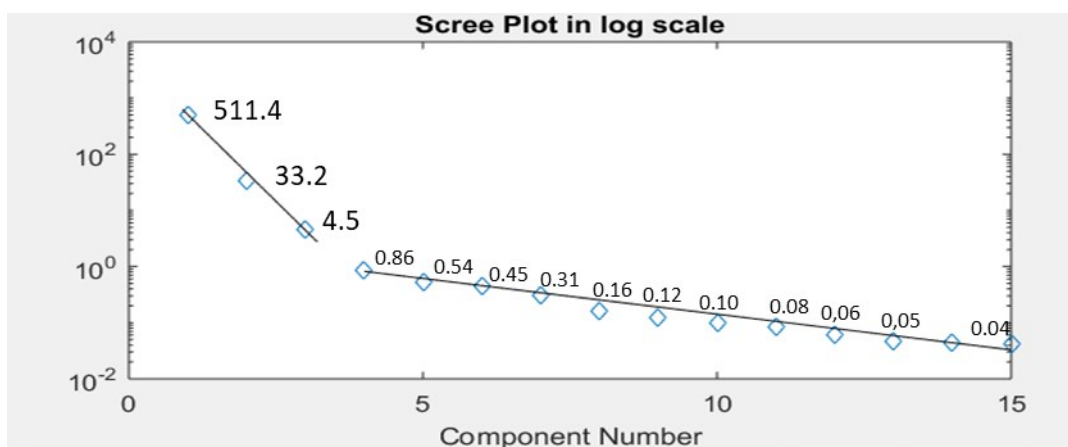


Fig. S5 PCA evaluation of the number of components explaining most of the variance contained in the data set (D) recorded during the activation of the bimetallic LDH precursor at the Ni K edge and presented in Figure 1a using the logarithm-scale representation of the Scree plot. The break slope is found between the third component and the fourth ones suggesting that 3 components are required to explain most of the variance contained in the matrix D.

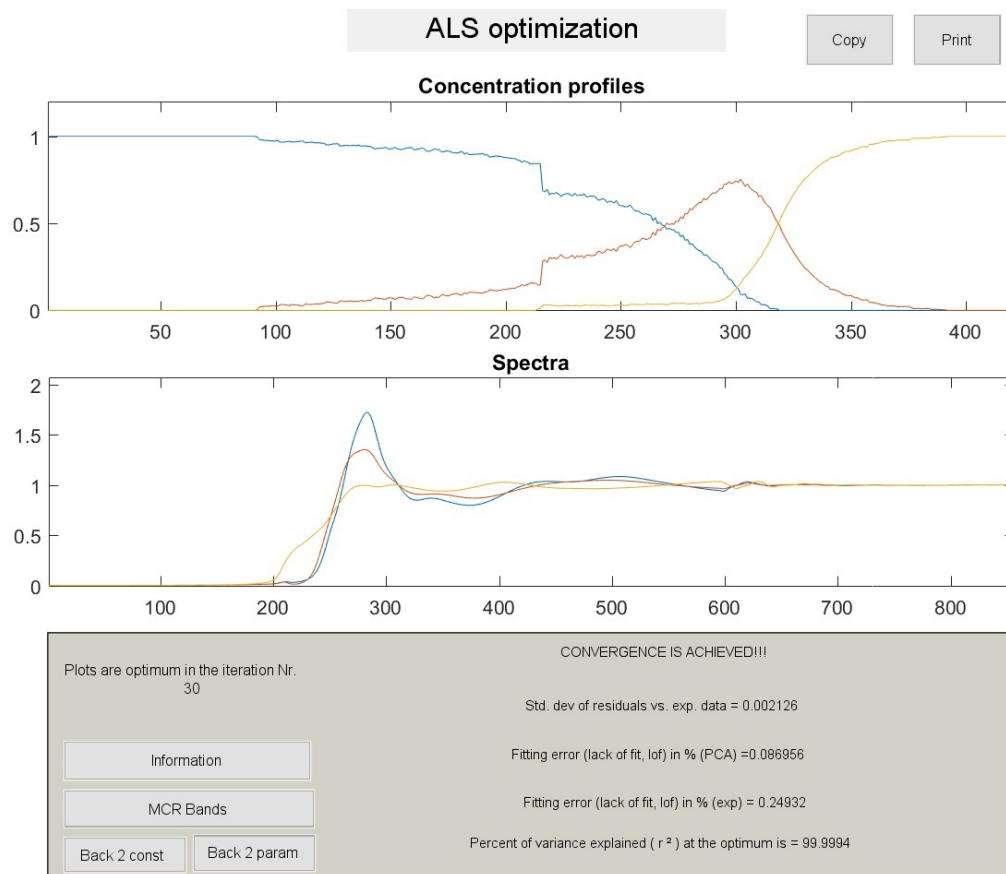


Fig. S6 Results of the minimization by MCR-ALS of the XAS data recorded at the Ni Kedge for the 2-stepped activation of the bimetallic LDH-precursor and presented in Figure 1a.

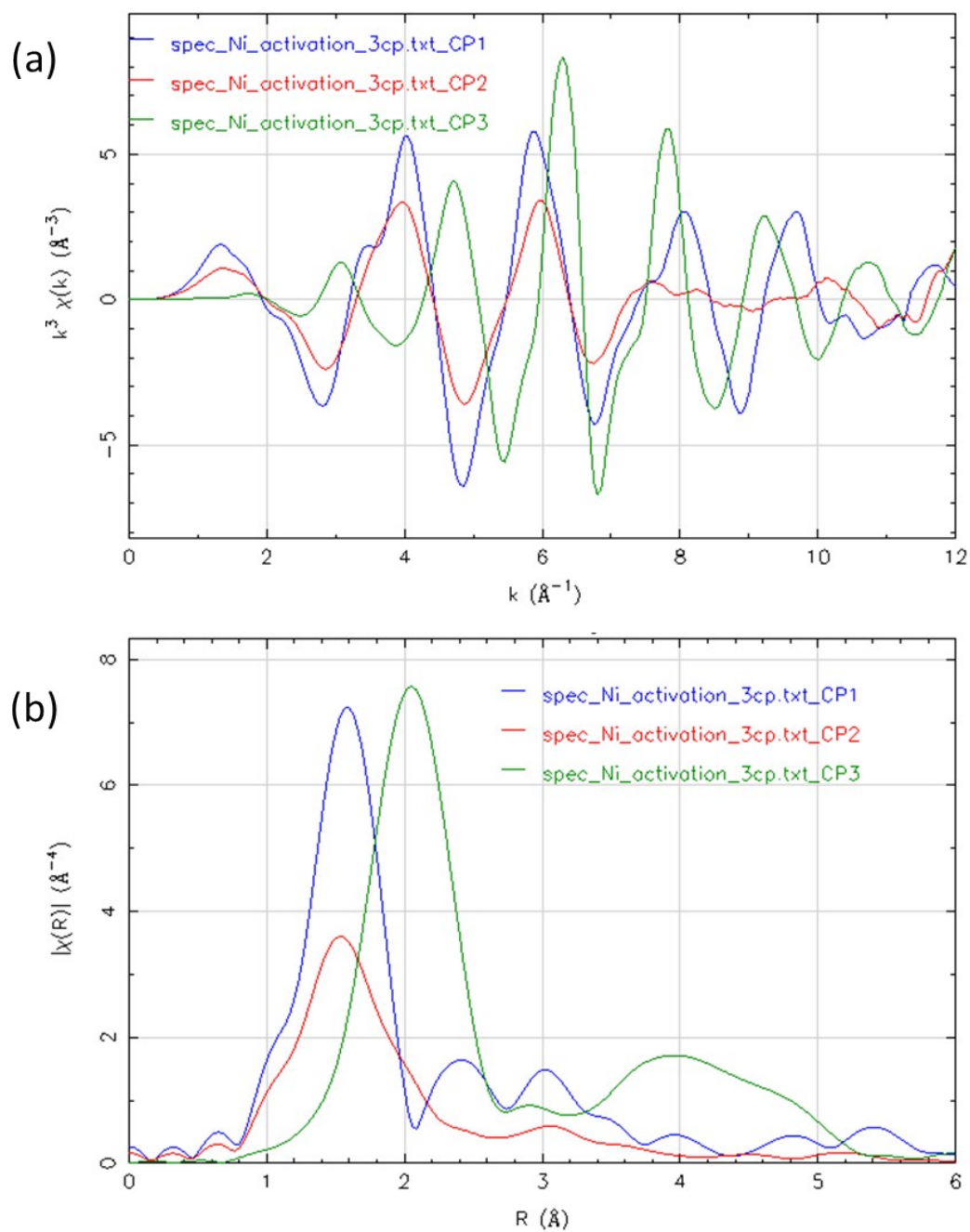


Fig. S7 (a) EXAFS spectra and (b) Fourier Transforms of the EXAFS spectra of the 3 components extracted by MCR-ALS analysis of the Ni K edge Quick-EXAFS data presented in Figure 1a.

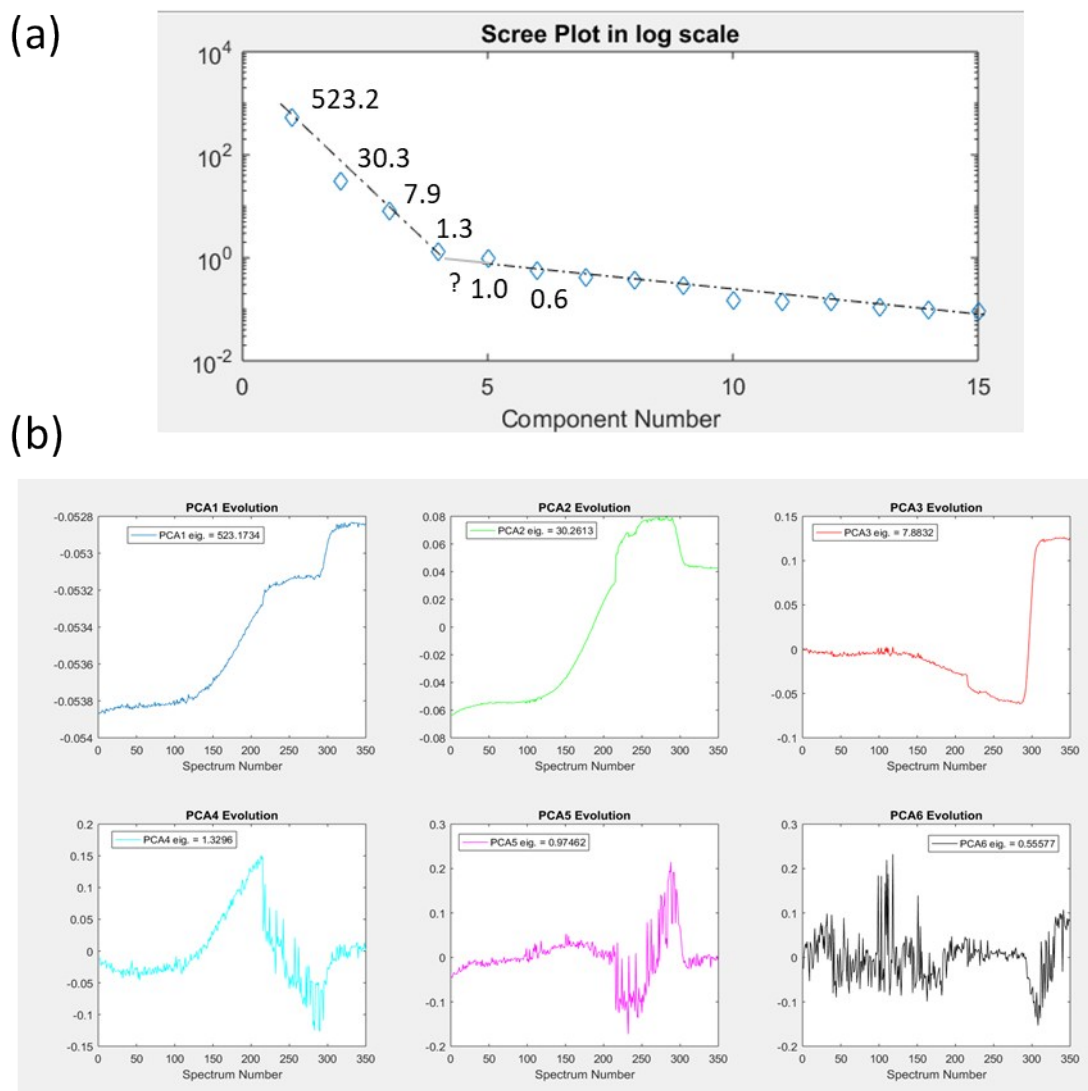


Fig. S8 PCA evaluation of the number of components explaining most of the variance contained in the data set recorded during the activation of the bimetallic LDH precursor at the Cu K edge and presented in Figure 1b.

a) Logarithm-scale representation of the Scree plot. The break slope is found between the third component and the fourth ones suggesting that 3 components are required to explain most of the variance contained in the matrix D.

b) Representations of the Scores for the first 6 components determined by SVD as a function of the number of spectra contained in the matrix D. Smooth trajectories for the first 3 components are observed but the 4th one could be also significant.

For the data recorded at the Cu K edge, the Scree plot or Score trajectory plot show unclear transit point.

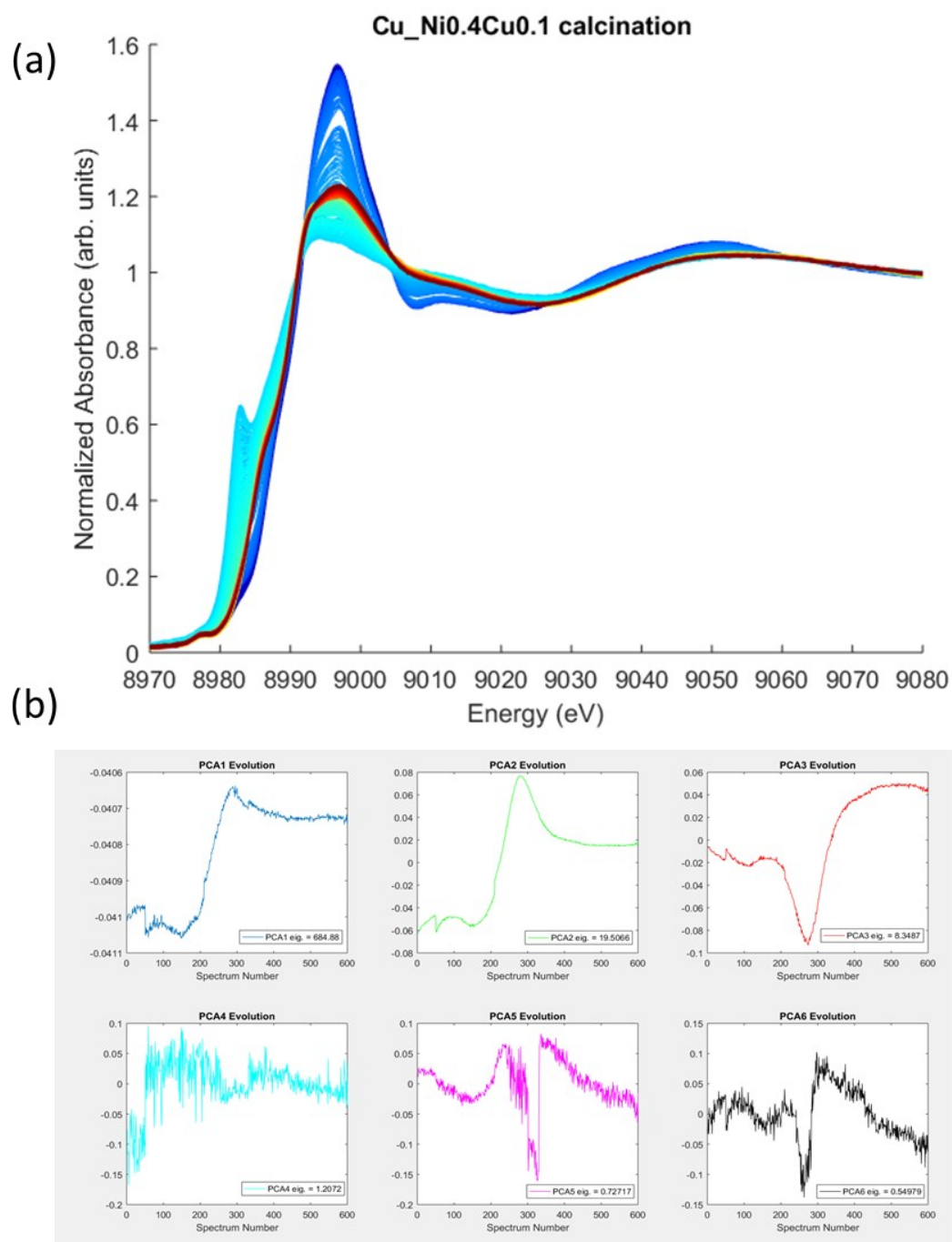


Fig. S9 (a) Cu K edge XAS data recorded during the calcination of the NiCu-LDH-precursors by heating the sample under air from RT (deep blue curves) to 500 °C (deep red curves). (b) Representations of the Scores for the first 6 components determined by SVD as a function of the number of spectra contained in the matrix D . Smooth and noise-less trajectories for the first 3 components are unambiguously observed.

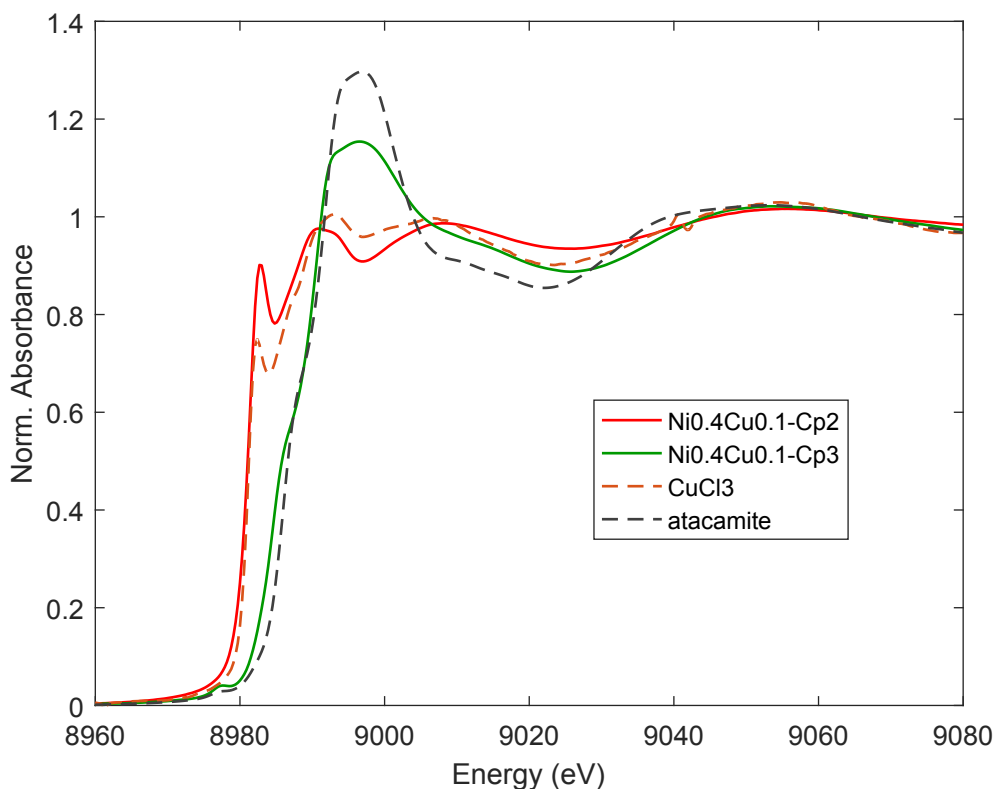


Fig. S10 Comparison of the Cu K edge XANES spectra extracted by MCR-ALS for the 2nd and 3rd components isolated during the calcination of the NiCu-LDH precursor by heating the sample under air from RT to 500 °C with experimental spectra recorded for a solution of the CuCl_3^{2-} complex⁴ and for the atacamite $\text{Cu}(\text{OH})_3\text{Cl}$ species. The solution of the the CuCl_3^{2-} complex was prepared by dissolving anhydrous CuCl into HCl ($\text{pH} = 1$) solution in the presence of NaCl (3 M ionic strength).⁵ The comparison of the XANES spectrum of the 2nd component with the one of CuCl_3^{2-} indicates the formation of a monovalent Cu species surrounded by chlorine ligands. The shape of the XANES spectrum of the 3rd component and the position of the rising edge is very similar to the one measured for the atacamite reference, evidencing the formation of a divalent Cu species with local order close to the one presented by atacamite.⁶

Table S1. Best fitted EXAFS parameters. N: coordination number, R: atomic distance from the absorbing atom, σ^2 : square of the Debye-Waller factor. R_f measures the relative misfit of the theory with respect to the experimental spectrum. $S_0^2 = 0.775$ and $E_0 = 8981$ eV.

		N	R (Å)	$\sigma^2 (10^{-3} \text{Å}^2)$	R_f (%)
NiCu-Cp2	Cu-Cl	2.0 ± 0.3	2.17 ± 0.02	8.5 ± 1.2	0.01354

* k-range = 3.4 – 9.7 Å⁻¹ R-range = 1.0 – 2.3 Å

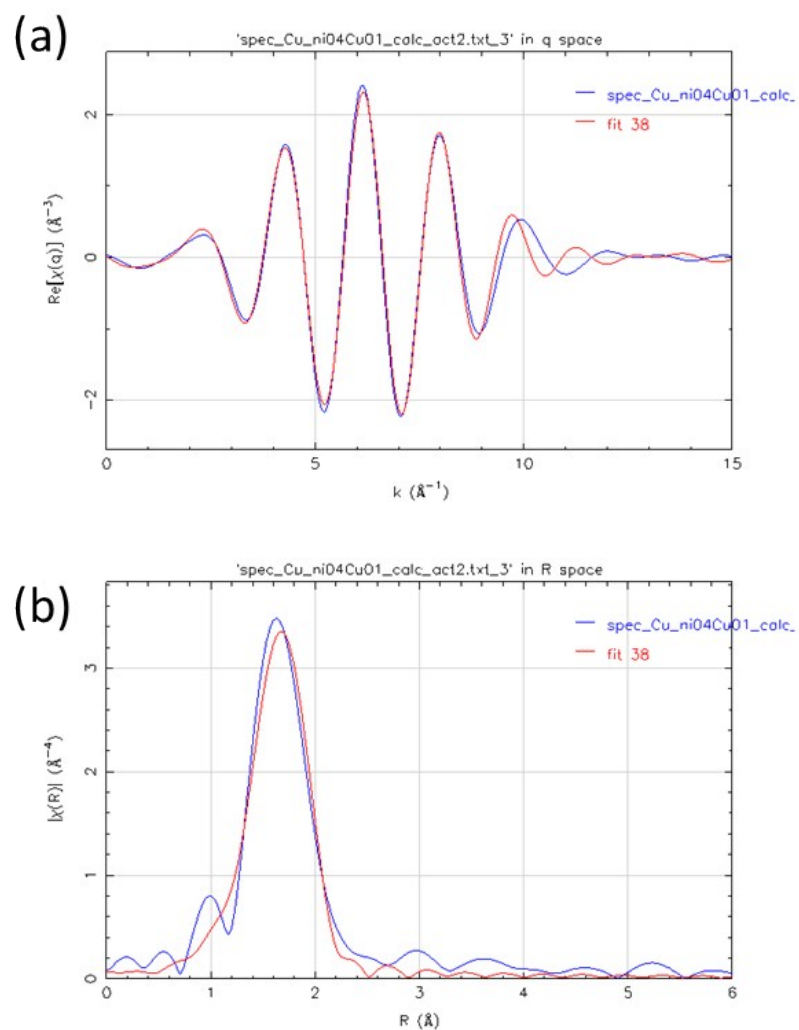


Fig. S11 Simulation of the Cu K edge EXAFS spectrum extracted by MCR-ALS for the 2nd component isolated during the calcination of the NiCu-LDH precursor by heating the sample under air from RT to 500 °C. (a) EXAFS spectra and (b) corresponding FT. The structural parameters so-obtained are gathered in Table S1. The Cu-Cl distance is compatible with the formation of the CuCl_2^- complex.⁷

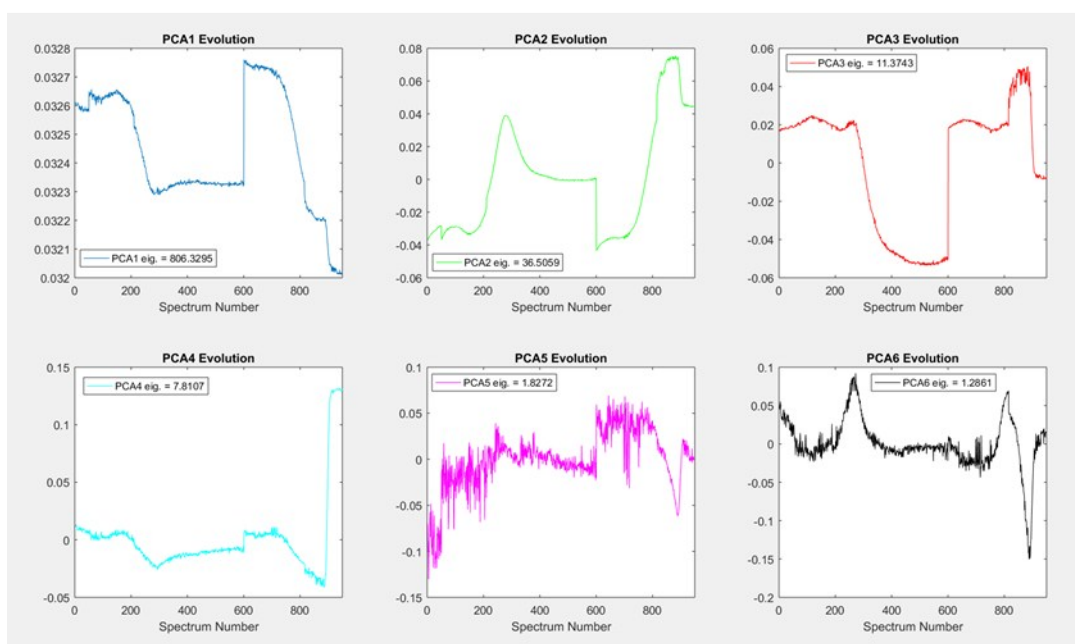
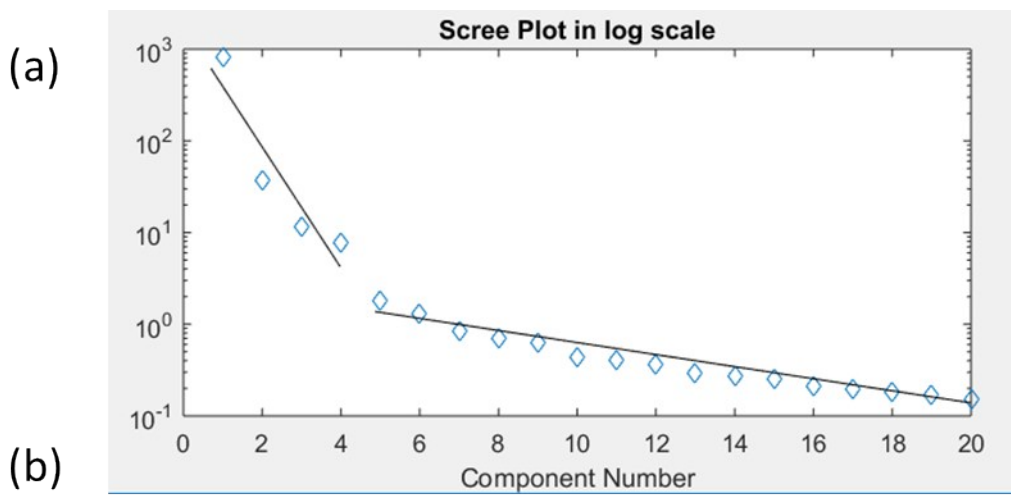


Fig. S12 PCA evaluation of the number of components necessary to explain most of the variance contained in the matrix D obtained by the concatenation of the XAS data recorded at the Cu Kedge during the calcination (spectra from 1 to 600) and those recorded during the 2-stepped activation of the bimetallic LDH-precursors (spectra 601 to 950).

a) Logarithm-scale representation of the Scree plot. The break slope is found between the fourth component and the fifth ones suggesting that 4 components are required to explain most of the variance contained in the matrix D.

b) Representations of the Scores for the first 6 components determined by SVD as a function of the number of spectra contained in the matrix D. Smooth trajectories for the first 4 components are observed.

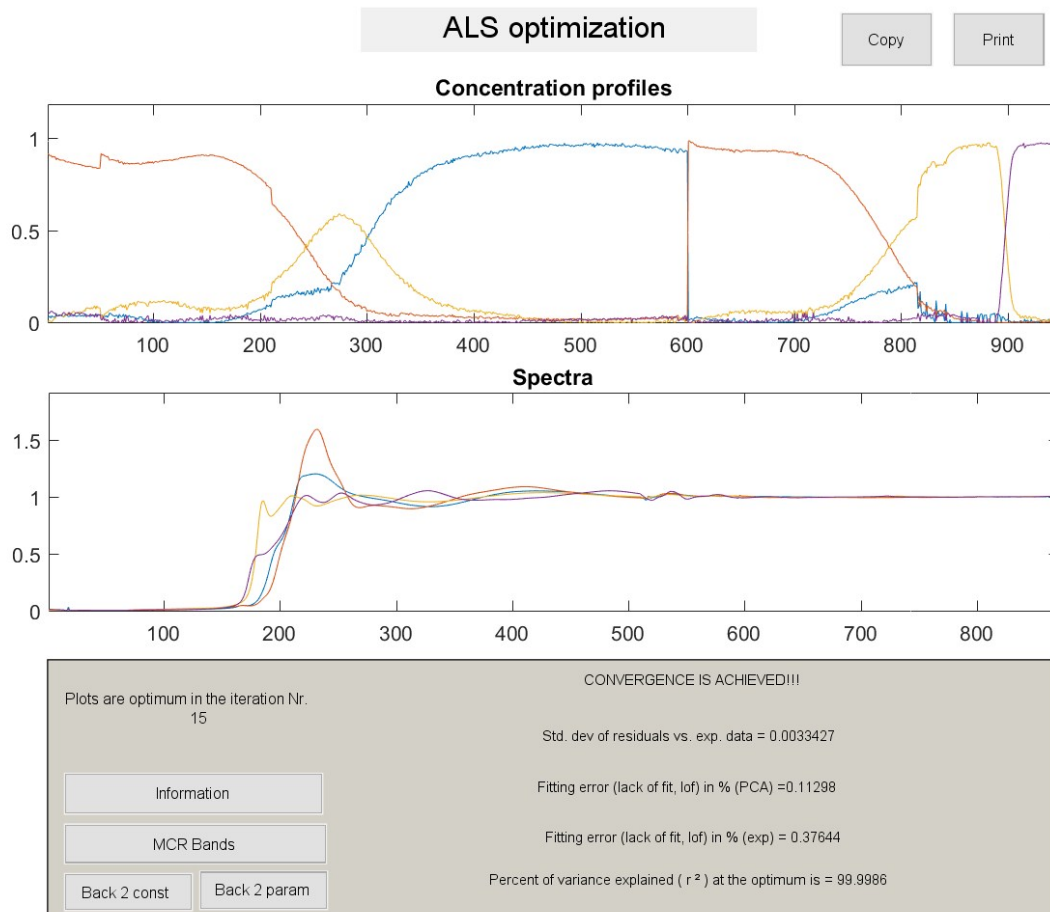


Fig. S13 Results of the minimization by MCR-ALS of the matrix obtained by the concatenation of the XAS data recorded at the Cu Kedge during the calcination (spectra from 1 to 600) and those recorded during the 2-stepped activation of the bimetallic LDH-precursors (spectra 601 to 950).

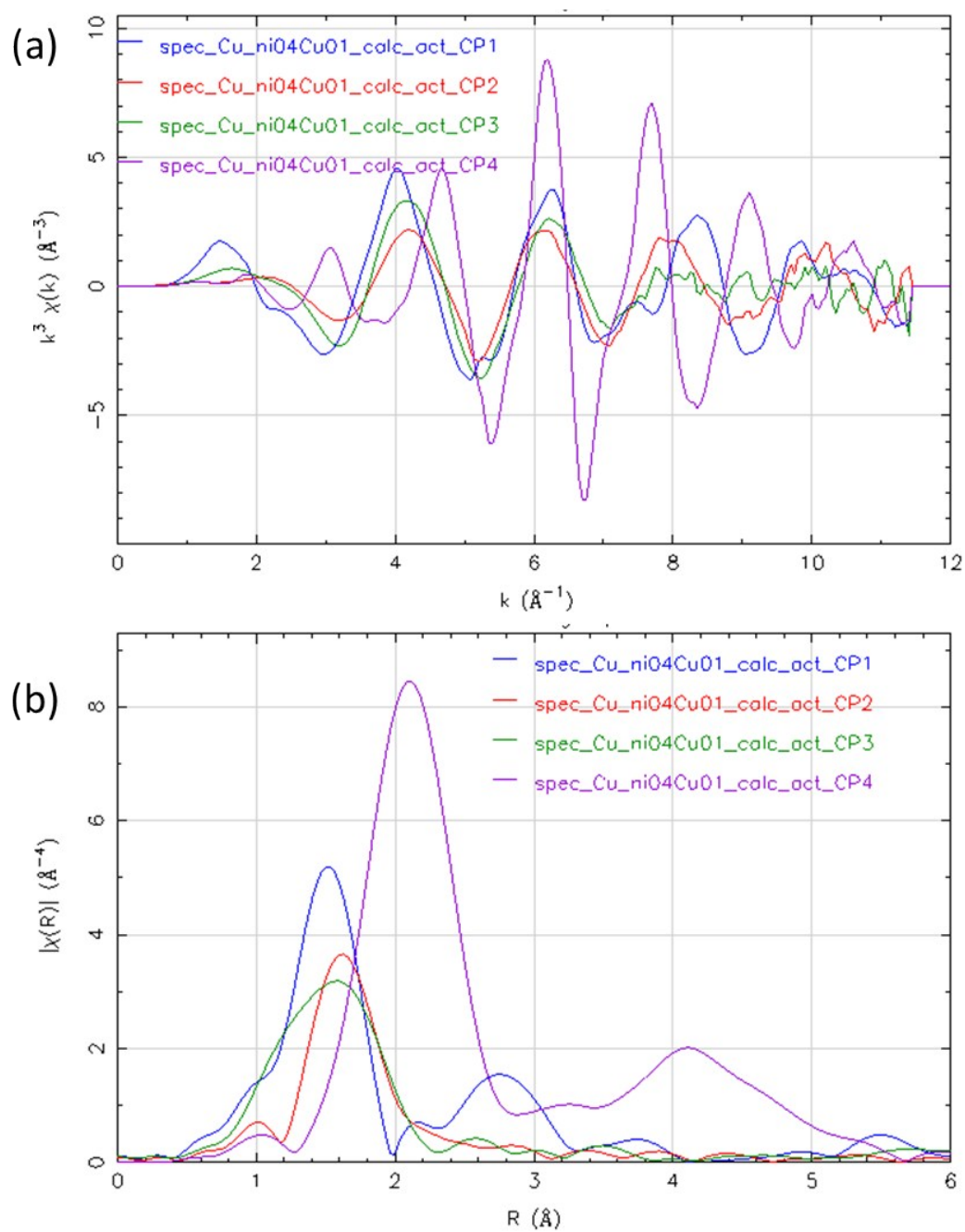


Fig. S14 (a) EXAFS spectra and (b) Fourier Transforms of the EXAFS spectra of the 4 components extracted by MCR-ALS analysis of the matrix obtained by the concatenation of the XAS data recorded at the Cu Kedge during the calcination and those recorded during the 2-stepped activation of the bimetallic LDH-precursors.

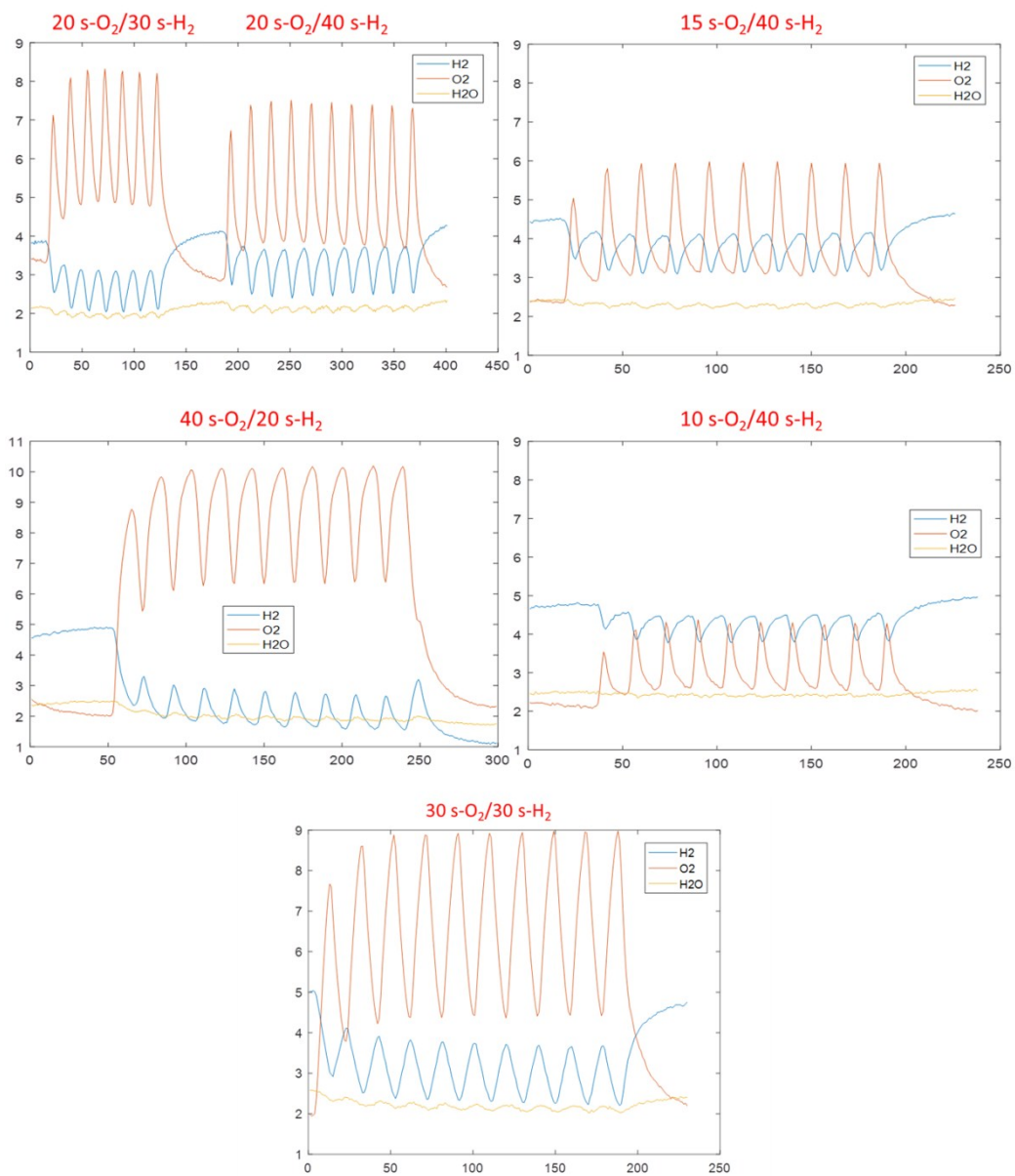


Fig. S15 Evolution of the MS signals for H₂, O₂ and H₂O at the outlet of a capillary filled with diamond for different pulse sequences.

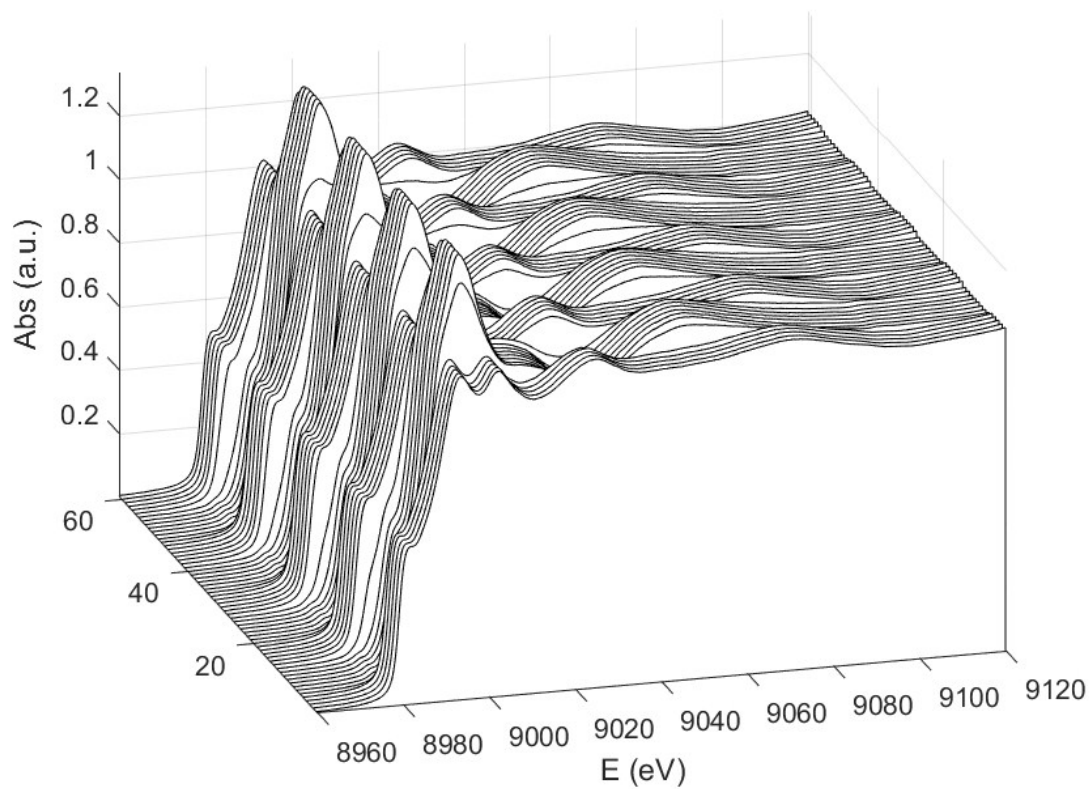


Fig. S16 3D evolution of the Cu K edge XANES spectra recorded for the $\text{Cu}_{0.5}$ activated catalyst under the pulse sequence 30 s- O_2 /30 s- H_2 . 10 successive quick-XAS spectra were merged in the pulse treatment leading to 5s of time resolution.

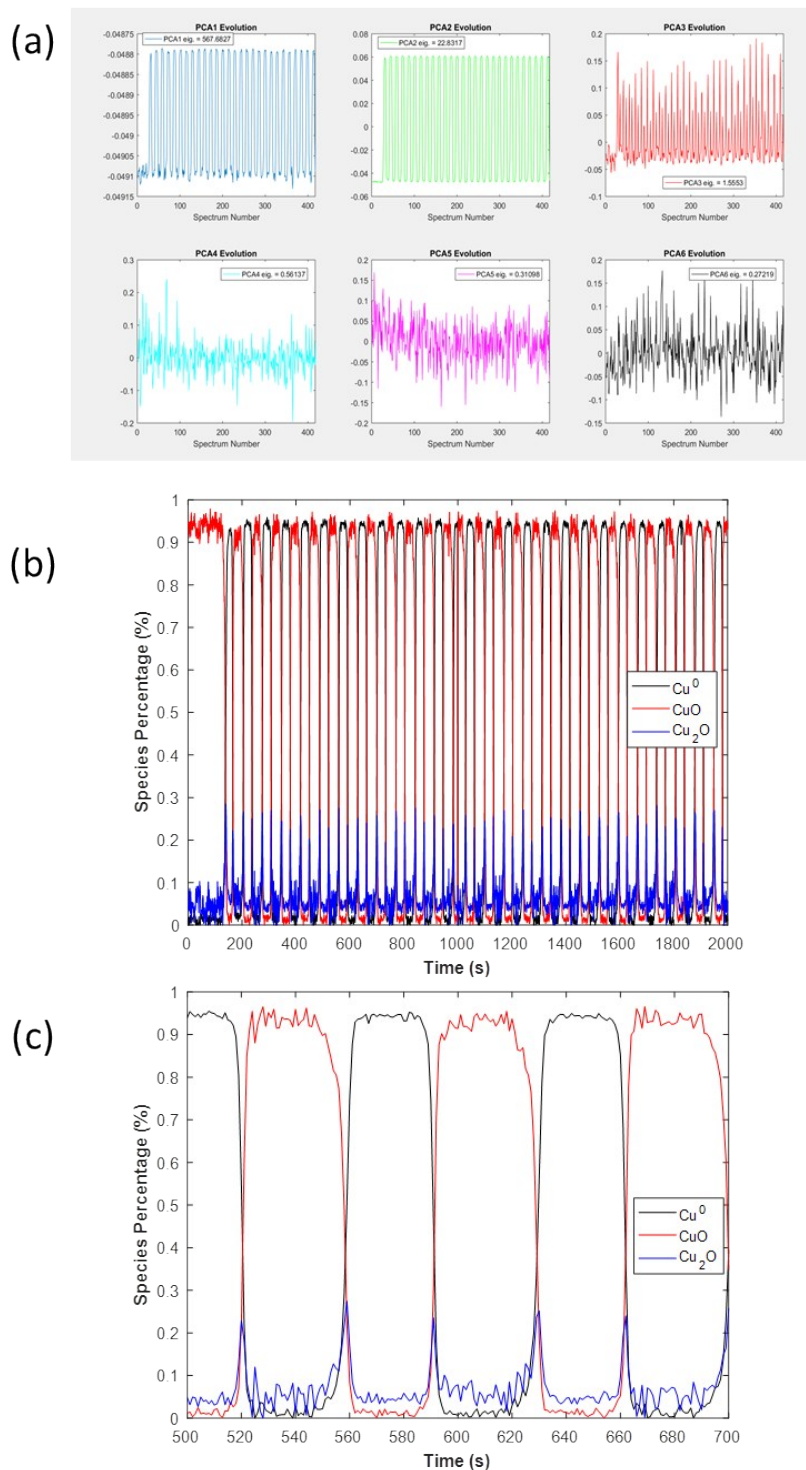


Fig. S17 (a) PCA evaluation of the number of components necessary to explain most of the variance contained in the matrix of Cu K edge quick-XAS spectra recorded during the 30 s-O₂/30 s-H₂ pulse sequence for the Cu_{0.5} activated catalyst (time resolution 5s). Pulsed trajectories of the Scores plot for the first 3 components are observed. (b) Concentration profiles obtained for the Cu K edge data recorded under 30 s-O₂/30 s-H₂ pulse sequence and (c) zoom over 200 s. The time resolution for the data reported in (b) and (c) is 1s (dealing with a merge of 2 successive spectra).

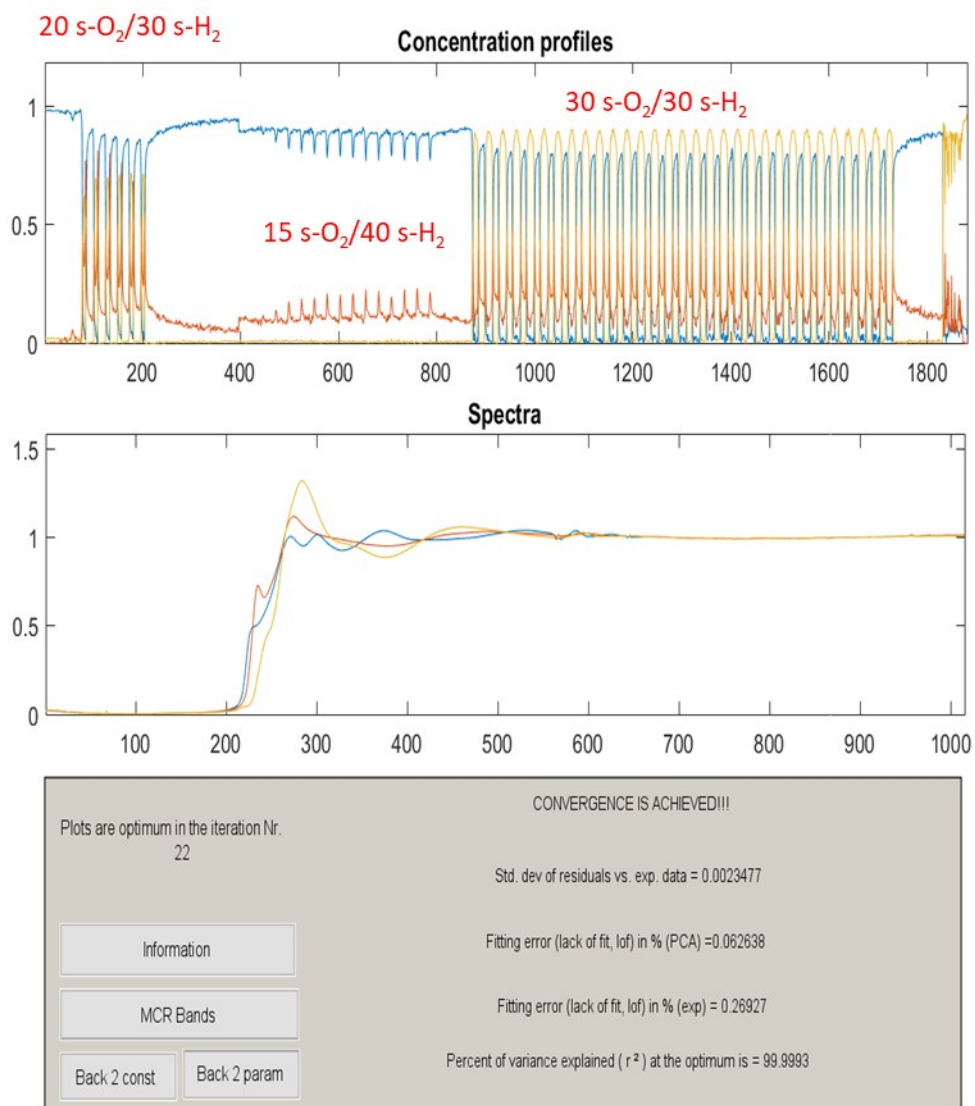


Fig. S18 Results of the minimization by MCR-ALS of the XAS data recorded at the Cu Kedge for Cu_{0.1} activated catalyst under different sequences of O₂/He and H₂/He pulses.

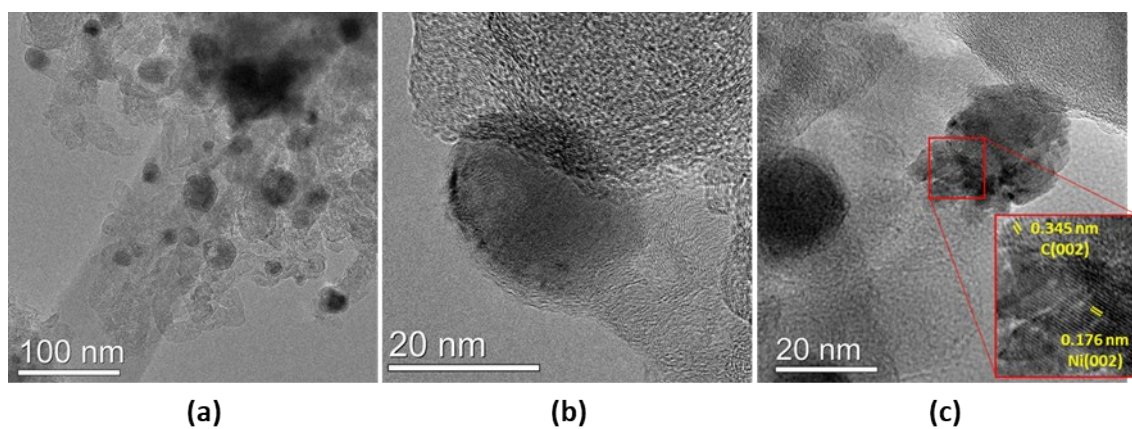


Fig. S19 (a) TEM and (b-c) HRTEM images of the spent Ni_{0.4}Cu_{0.1} catalyst.

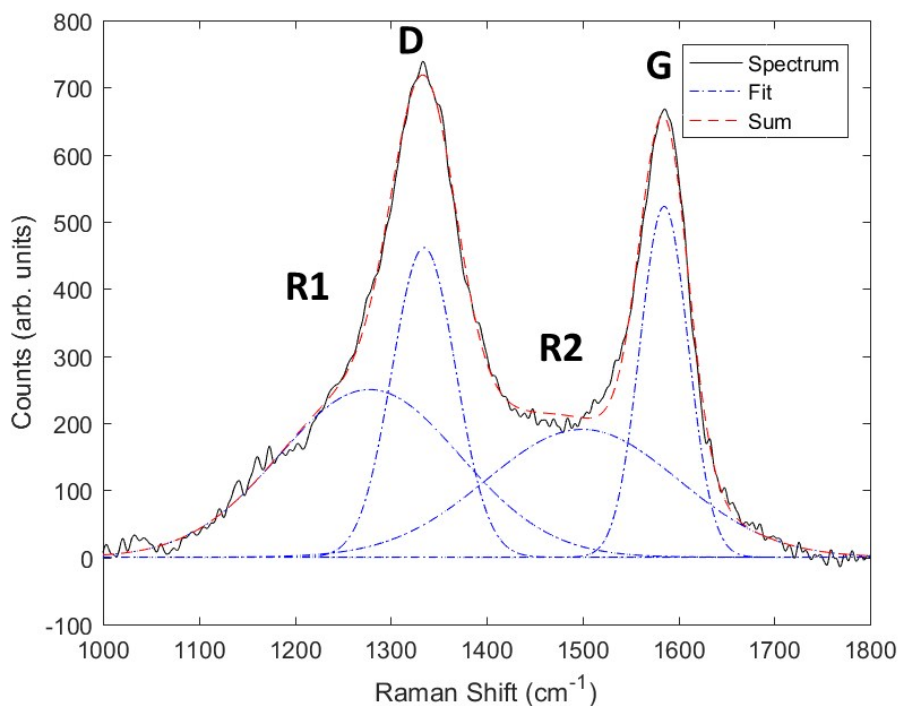


Fig. S20 Example of deconvolution of a Raman spectrum of the carbon deposits formed on the surface of the catalysts after the reaction. Lorentzian function was used for fitting D and G lines whereas Gaussian function was used for fitting R1 and R2 lines. The position of the R1 and R2 lines were fixed to 1278 and 1500 cm^{-1} , respectively, whereas the position of the two Lorentzian lines, the amplitude and width (FWHM) of the four lines were allowed to vary during the least square fitting.

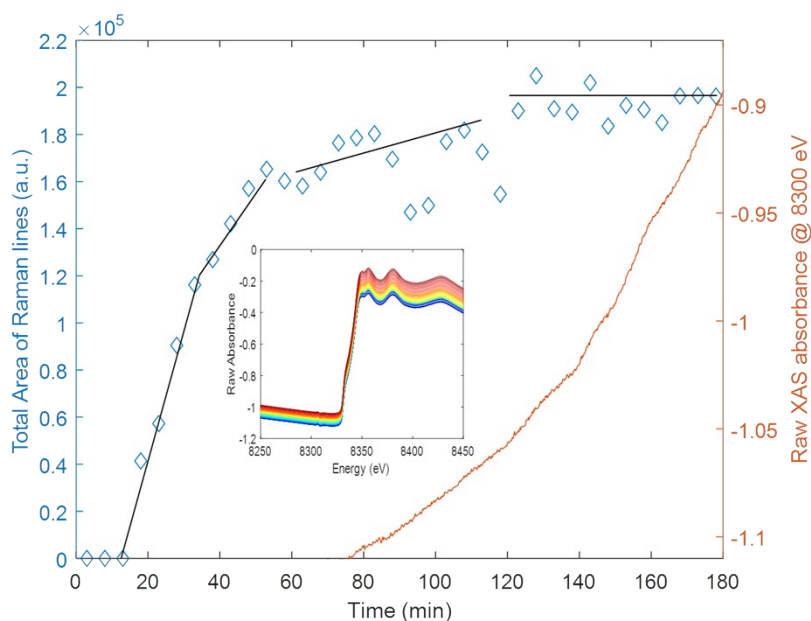


Fig. S21 Comparison of the total area of carbonaceous species (sum of areas of D, G, R1 and R2 lines) measured during the first ESR with the change of the level of raw XAS absorbance at 8300 eV measured simultaneously with Raman. The inset displays the raw XAS spectra measured

upon TOS (time is increasing from the blue to the red spectra) from which is determined the red curve. Raman probe depth is related to the penetration depth of the laser which is typically of a few microns. When the thickness of the carbon layer is larger than the laser penetration depth, invariance of the total area of carbonaceous species (sum of area of D, G, R1 and R2 bands) is observed as presented in Fig. S21. This figure in comparison with ethanol conversion for the first ESR treatment shown in Fig. 6a evidences that 4 steps characterize the coke formation during the first ESR reaction: i) for $t < 18$ min, no coke deposits are formed and ethanol conversion is stable, ii) for $18 \text{ min} \leq t \leq 53$ min, a rapid increase of total area is observed with little impact on conversion, iii) for $58 \text{ min} \leq t \leq 113$ min, the area starts to be stabilized with a slight increase of 13% observed between 113 and 58 minutes, conversion of ethanol decreases from 98 % to 92 %, iv) for $118 \text{ min} \leq t \leq 180$ min, the area is stable but conversion of ethanol still decreases because coke is still produced. The formation of coke is evident from the increase of the raw XAS spectra measured upon TOS (inset of the figure, time is increasing from the blue to the red spectra) indicating that the transmission of the sample decreases due to carbon deposits at the surface of the support. In particular, the raw XAS absorbance (red curve – γ_{axis} right) measured at 8300 eV in the time period where nearly no more evolution of the total area of Raman lines is observed is the complementary evidence of coke formation.

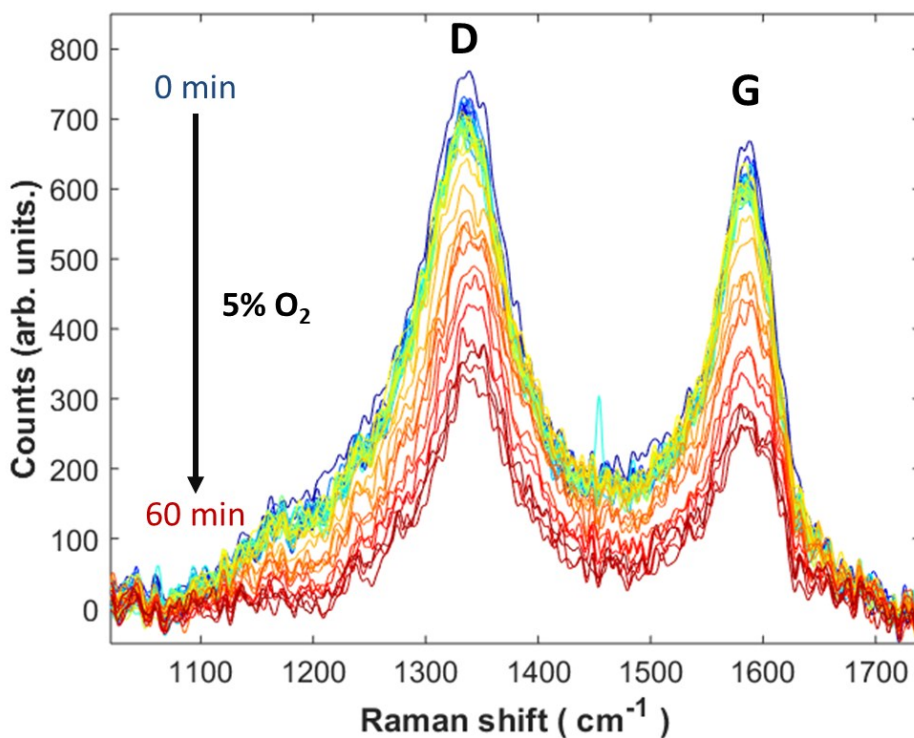


Fig. S22 Raman spectra simultaneously measured during the regeneration under 5% O₂/He of the spent catalyst after the first ESR reaction.

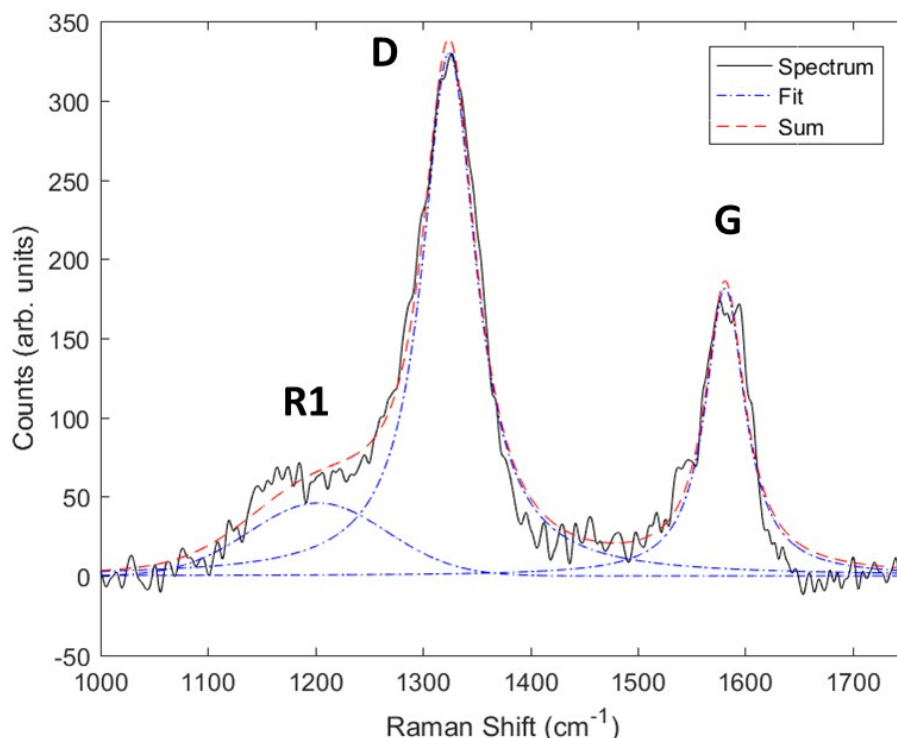


Fig. S23 Deconvolution of the difference spectrum obtained by subtracting the spectra presented in Figure 12 which were recorded at the end of the second ESR reaction and at the end of the regeneration. The deconvolution was carried out with 3 lines: two Lorentzian (D and G) lines and one Gaussian line (R1). Position, amplitude and width were allowed to vary.

Table S2. Parameters used for the deconvolution of the experimental Raman spectra reported in Fig. 12 and Fig. S21. Lorentzian function was used for fitting the D and G lines whereas Gaussian function was used for fitting R1 and R2 lines. The percentage of a given line is obtained by calculating the ratio between the area of this line over the cumulative area of the four lines. The D/G ratio is the ratio between the relative percentage of the D and G lines.

Sample	R1		D		R2		G		D/G
	Center cm ⁻¹	%	Center cm ⁻¹	%	Center cm ⁻¹	%	Center cm ⁻¹	%	
End of ESR1	1278	20.1	1333.1 ± 0.5	42.3	1500	8.2	1585.8 ± 0.3	29.5	1.43
End of Regeneration	-	-	1342.8 ± 0.6	60.0	1500	3.4	1584.1 ± 0.9	36.6	1.64
End of ESR2	1278	9.7	1333.9 ± 0.5	55.8	1519	4.7	1584.6 ± 0.5	29.8	1.87
Difference spect. (Fig. S22)	1200.3 ± 7.6	15.1	1324.6 ± 0.6	60.5	-	-	1581.3 ± 0.8	24.4	2.48

References

- 1 A. R. Passos, S. H. Pulcinelli, C. V. Santilli and V. Briois, *Catal. Today*, 2019, **336**, 122–130.
- 2 Y. J. Liu, T. Tran, G. Postma, L. M. C. Buydens and J. Jansen, *Anal. Chim. Acta*, 2018, **1020**, 17–29.
- 3 C. Lesage, E. Devers, C. Legens, G. Fernandes, O. Roudenko and V. Briois, *Catal. Today*, 2019, **336**, 63–73.
- 4 H. W. P. Carvalho, S. H. Pulcinelli, C. V. Santilli, F. Leroux, F. Meneau and V. Briois, *Chem. Mater.*, 2013, **25**, 2855–2867.
- 5 N. Reddy, P. Bera, V. R. Reddy, N. Sridhara, A. Dey, C. Anandan and A. K. Sharma, *Ceram. Int.*, , DOI:<http://dx.doi.org/10.1016/j.ceramint.2014.03.133>.
- 6 J. B. Parise and B. G. Hyde, *Acta Crystallogr.*, 1986, **C42**, 1277–1280.
- 7 J. Brugger, B. Etschmann, W. Liu, D. Testemale, J. L. Hazemann, H. Emerich, W. van Beek and O. Proux, *Geochim. Cosmochim. Acta*, 2007, **71**, 4920–4941.